A non-local hydrodynamic model for the shear viscosity of confined fluids: analysis of a homogeneous kernel

2008 J. Phys. A: Math. Theor. 41 035501

(http://iopscience.iop.org/1751-8121/41/3/035501)

IOP PUBLISHING JOURNAL OF PHYSICS A: MATHEMATICAL AND THEORETICAL

J. Phys. A: Math. Theor. **41** (2008) 035501 (23pp) doi:10.1088/1751-8113/41/3/035501

A non-local hydrodynamic model for the shear viscosity of confined fluids: analysis of a homogeneous kernel

Peter J Cadusch[1], B D Todd[2], Junfang Zhang[3] and Peter J Daivis[4]

[1] Faculty of Engineering and Industrial Sciences, Swinburne University of Technology, PO Box 218, Hawthorn, Victoria 3122, Australia
[2] Centre for Molecular Simulation, Swinburne University of Technology, PO Box 218, Hawthorn, Victoria 3122, Australia
[3] CSIRO Petroleum Resources, Ian Wark Laboratory, Bayview Avenue, Clayton, Victoria 3168, Australia
[4] Applied Physics, School of Applied Sciences, RMIT University, GPO Box 2476V, Melbourne, Victoria 3001, Australia

E-mail: btodd@swin.edu.au

Received 15 June 2007, in final form 26 October 2007
Published 4 January 2008
Online at stacks.iop.org/JPhysA/41/035501

Abstract

We present a detailed analysis of a hydrodynamic constitutive model recently applied to study the non-local viscosity of highly confined inhomogeneous fluids (Zhang *et al* 2004 *J. Chem. Phys.* **121** 10778, Zhang *et al* 2005 *J. Chem. Phys.* **122** 219901). This model makes the assumption that, for pore widths significantly greater than the width of the viscosity kernel, one can approximate the true inhomogeneous kernel with a homogeneous kernel. We test this assumption with a simple mathematical model that mimics the simulation scheme of Zhang *et al*. Our analysis shows that the assumption of a homogeneous non-local viscosity kernel is reasonable for low density fluids confined to relatively large pore widths (channel separation distances) but becomes less reliable for higher density fluids and smaller channel separations. We find that the extraction of the viscosity kernel is not simple because of the lack of information about the stress response function at the fluid–wall boundaries. This lack of information can lead to singularities in the kernel and can also distort its shape. As a concluding remark, we also suggest a methodology which avoids these problems.

PACS numbers: 05.10.−a, 05.60.−k, 61.46.–w, 66.20.+d, 82.20.Wt, 83.10.Gr

1. Introduction

Recently an attempt was made to use a hydrodynamic constitutive equation to extract a non-local viscosity for highly confined inhomogeneous nonequilibrium fluids [1]. It has been known for some time that Newton's law of viscosity, computed as the ratio of the *local* shear stress to the *local* value of the strain rate, breaks down when the degree of confinement is of the order of the range of the intermolecular potential and where significant variations in the strain rate occur over this length scale. One can show that use of this local definition for the viscosity in a highly confined fluid can result in singularities in the local viscosity [1, 2]. It is important to appreciate that these local singularities are not the result of mathematical manipulations that might be amenable to renormalization techniques. They are the result of an inappropriate definition of the viscosity, namely that it is a local function of strain rate and stress. Evans and Morriss [3] proposed a simple linear non-local constitutive equation that might be useful for a homogeneous fluid where the strain rate varies appreciably over the range of the interaction potential, yet the fluid remains uniform in density. Such a situation may occur, for example, in simulations of a fluid under the influence of an external sinusoidal transverse force in the weak field limit (under strong fields, the fluid itself develops strong inhomogeneities). Their equation was proposed as

$$P_{yx}(\mathbf{r}, t) = -\int_0^t \mathrm{d}s \int_{-\infty}^{\infty} \mathrm{d}\mathbf{r}'\, \eta(\mathbf{r} - \mathbf{r}', t - s)\dot{\gamma}(\mathbf{r}', s) \tag{1}$$

where P_{yx} is the negative of the shear stress, η is the non-local viscosity kernel and $\dot{\gamma}$ is the strain rate, defined as $\dot{\gamma}(y, t) = \partial u_x(y, t)/\partial y$, where in what follows the fluid is assumed to be flowing in the x direction with a gradient in the y direction only. In equation (1) the simple proportionality between stress and strain rate implicit in Newton's law and its local generalization has been replaced by a double convolution in space and time so that the stress at position $\mathbf{r}$ and time t is not simply proportional to the strain rate at position $\mathbf{r}$ and time t, but is proportional to the entire strain rate history, and strain rate distribution across the fluid. What this means in practical terms is that all liquids have a memory effect and therefore behave viscoelastically.

For fluids that are strongly inhomogeneous, equation (1) needs to be reformulated to account for the fact that the viscosity kernel depends not just on the relative distance between two points in the fluid $(\mathbf{r} - \mathbf{r}')$ but also on the absolute point in space, $\mathbf{r}$, from which the relative distances can be measured. This accounts for the lack of translational invariance in an inhomogeneous fluid. Thus, the kernel can be written as $\eta(\mathbf{r}, \mathbf{r} - \mathbf{r}', t - s)$, and the simplest general linear constitutive equation for this purpose may be expressed as

$$P_{yx}(\mathbf{r}, t) = -\int_0^t \mathrm{d}s \int_{-\infty}^{\infty} \mathrm{d}\mathbf{r}'\, \eta(\mathbf{r},\ \mathbf{r} - \mathbf{r}', t - s)\dot{\gamma}(\mathbf{r}', s). \tag{2}$$

Currently there is no known method of extracting the viscosity kernel defined in equation (2) from either experimental or simulation data for an inhomogeneous confined fluid. To simplify the problem, Zhang *et al* [1] proposed that an *effective* viscosity profile may at least provide an estimate of the average viscosity over the pore, bearing in mind that a local definition of the viscosity is fundamentally flawed. Mathematically, the assumption of an effective viscosity kernel is, in its simplest manifestation, equivalent to writing the viscosity kernel as a *homogeneous* function of relative separation, i.e. $\eta(\mathbf{r}, \mathbf{r} - \mathbf{r}', t - s) \approx \eta(\mathbf{r} - \mathbf{r}', t - s)$. Such an assumption is likely to be reasonable sufficiently far from the walls for relatively low density fluids and/or for flows in channels whose width is significantly larger than the

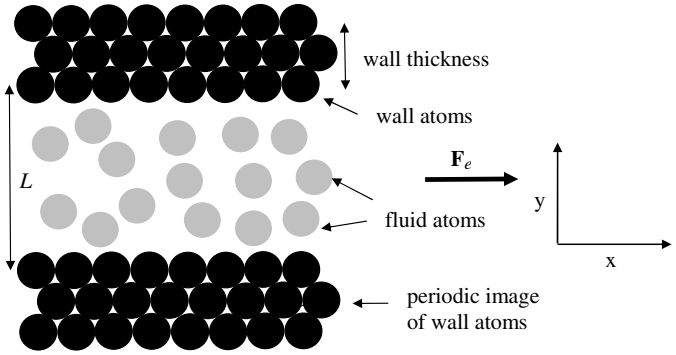

Figure 1. Geometry of the simulation environment, showing wall and fluid atoms (z-direction normal to page). A time-independent external field $\mathbf{F}_e$ in the x-direction drives the fluid to a nonequilibrium steady state.

effective length scale of the kernel. If one makes this assumption and also considers only steady-state flows then equation (2) becomes

$$P_{yx}(y) = -\int_{-\infty}^{\infty} \mathrm{d}y'\, \eta(y - y')\dot{\gamma}(y') \tag{3}$$

bearing in mind the geometry of the flow as discussed above. The form of equation (3) now allows one to extract the viscosity kernel by a sequence of simple steps: (1) Fourier transforming equation (3) to obtain

$$\tilde{\eta}(k_y) = -\tilde{P}_{yx}(k_y)/\tilde{\dot{\gamma}}(k_y), \tag{4}$$

where the tilde above a quantity denotes the Fourier transform of that quantity and k_y is the wavenumber; (2) taking discrete Fourier transforms (DFTs) of the simulated data for the shear stress ($P_{yx}(y)$) and strain rate ($\dot{\gamma}(y)$) to obtain $\tilde{P}_{yx}(k_y)$ and $\tilde{\dot{\gamma}}(k_y)$ respectively; (3) substituting $\tilde{P}_{yx}(k_y)$ and $\tilde{\dot{\gamma}}(k_y)$ into equation (4) to obtain the transformed viscosity kernel; and finally (4) inverse Fourier transforming the k-space kernel into real space.

It is important to appreciate that equations (1)–(3) have been proposed as a possible model for transport for inhomogeneous flows for a number of years [2, 4, 5], but until the recent work of Zhang *et al* [1] had never actually been tested. We note that non-local theories have been used in the modelling of stress in Brownian suspensions of rigid fibres [6] as well as transport in plasmas [7]. We also note that non-local formalisms are invoked in theories of generalized hydrodynamics [8–11], though these are almost always confined to the case of homogeneous fluids. However for the specific application presented here, it is clear that a deeper understanding of the problem still needs to be arrived at, and it is in this spirit that the current paper is presented. We ask ourselves: to what extent is the assumption of a homogeneous viscosity kernel a reasonable approximation for an effective non-local viscosity in a highly confined fluid?

To set the stage for the analysis that follows in subsequent sections we will consider a model three-dimensional fluid confined in the y-direction undergoing planar Poiseuille flow (or, equivalently, gravity driven flow [12]) in the x-direction, as shown in figure 1. We will model the physical system with simple analytical functions that we can work with. We will then compare our analytic viscosity kernels with kernels extracted from actual molecular dynamics simulations of a confined fluid under Poiseuille flow. This analysis will shed significant light onto the difficult problem of computing a non-local viscosity from a hydrodynamic constitutive

equation for an inhomogeneous system. It must be said that despite the approximations involved (in particular the assumption of a homogeneous effective viscosity kernel and the use of equation (3) for a confined fluid), the solution of such a problem should be seen as a significant milestone in the viscoelastic theory of confined fluids, for it has been conclusively demonstrated that the assumption of a local viscosity for such fluids is grossly incorrect [1, 2, 4, 5].

The remainder of this paper is structured as follows. In section 2 we consider the problem at hand and demonstrate analytically by the aid of a simple mathematical model the types of difficulties that are likely to arise in the extraction of the viscosity kernel. In particular we examine in detail the effect that domain restriction has on the de-convolution of equation (3). In section 3 we describe our molecular dynamics simulations and compare the results of our extracted simulation viscosity kernels with those of the simple mathematical model, particularly the shapes of the kernels. Finally, we summarize and conclude our analysis in section 4.

2. Effect of domain restriction on inverse convolution

2.1. Statement of the problem

A confined fluid implies that both the shear stress and strain rate are not infinite in extent but remain non-zero only over some limited domain, $y \in (-a, a)$ where $a = L/2$ and L is the effective channel width. Provided that no significant penetration of fluid into the walls occurs, then both these quantities are undefined outside the range of confinement, either in a real experiment or in a molecular dynamics simulation. It is also clear that equation (3) is only strictly true for a shift invariant system since the kernel is homogeneous. This could only ever be the exact case for an infinite homogeneous fluid. However, if the kernel has an effective length scale of ξ that is significantly less than a (i.e., $\eta(y)$ is effectively non-zero only over some range $|y| < \xi \ll a$) then equation (3) might be a useful approximation to the real kernel. Note that use of equation (3) implies that the non-local viscosity extracted is *not* a position-dependent non-local viscosity [1]. The only way the actual position dependence can be extracted is to consider modelling the system by equation (2), which essentially means building the density dependence into the model. We will address this more complex issue in a forthcoming article.

In molecular dynamics simulations of Poiseuille flow [1, 2, 4, 12] the shear stress and strain rate are essentially linear functions, upon which are superimposed harmonic oscillations that result from the fluid layering near the walls. These nonlinear oscillatory effects become more prominent as either the fluid density increases or the channel width decreases. For the purposes of our mathematical model, if we ignore this corrugation then both the shear stress and strain rate have linear ramp-like forms:

$$P_{yx}(y), \ \dot{\gamma}(y) \sim A\, \Pi_a(y)\, y, \tag{5}$$

where A is a constant and $\Pi_a(y)$ is the top-hat function defined as

$$\Pi_a(y) = \begin{cases} 1; & |y| \leqslant a \\ 0; & |y| > a. \end{cases} \tag{6}$$

If the viscosity kernel has an effective length scale of $\xi \ll a$ then, apart from a region of size roughly ξ near the walls, the form of $P_{yx}(y)$ is essentially independent of the form of $\eta(y)$. This is because for an infinite system without walls, the convolution of a ramp function given by equation (5) is another ramp function with a slope given by the integral of the kernel

function $\eta(y)$ but which is independent of the exact shape of $\eta(y)$. In the presence of walls, one can show that the information about the kernel's shape is contained predominantly in the behaviour of $P_{yx}(y)$ near the fluid–wall boundaries (see appendix A). In itself this is not a problem as long as the complete stress response is available. Unfortunately this is not the case. Equation (5) implies that we only have knowledge of the stress response up to the walls and indeed this is all that we can obtain via molecular dynamics simulation [1, 12]. However, the natural support of a function defined by equation (3) extends beyond the walls, where by 'support' we mean the smallest interval, which contains the sub-domain over which the function is non-zero. This is simply a consequence of the non-local nature of the fluid with a finite non-zero viscosity kernel. The support of $P_{yx}(y)$ *defined* by equation (3) is given by the sum of the supports of the strain rate and viscosity kernel, i.e. $P_{yx}(y) \in (-a-\xi, a+\xi)$. In molecular dynamics simulations we have no knowledge of $P_{yx}(y)$ in the regions $-a-\xi \leqslant y < -a$ and $a < y \leqslant a+\xi$. This means that essentially half of the region affected by the convolution in a usable way is lost and a simple de-convolution based on the assumption that all the data are available will result in a kernel that is inaccurate. We demonstrate this as follows.

2.2. *Expected error in the kernel*

Assuming that the support of $\eta(y)$ is of the order ξ, then the true stress can be expressed as a linear sum of the available estimate $P^a_{yx}(y)$ with support $(a, -a)$ (i.e., what we can obtain from computer simulation of the confined fluid) and the missing information, $P^e_{yx}(y)$, with support $a < |y| \leqslant a+\xi$, i.e.,

$$P_{yx}(y) = P^a_{yx}(y) + P^e_{yx}(y) \quad \Rightarrow \quad P^a_{yx}(y) = P_{yx}(y) - P^e_{yx}(y). \tag{7}$$

Since the strain rate is an odd function of y and the kernel is an even function of y, the missing stress information has the form

$$P^e_{yx}(y) = b(y-a) - b(-(y+a)), \tag{8}$$

where b is a function and $b(y) = 0$ for $y < 0$. Since $b(y)$ is a real function, the Fourier transform of the error term can be expressed as

$$\tilde{P}^e_{yx}(k_y) = -2\mathrm{i}|\tilde{B}(k_y)| \sin\left[k_y a + \phi_{k_y}\right], \tag{9}$$

where $\tilde{B}(k_y)$ is the Fourier transform of $b(y)$ and ϕ_{k_y} is the argument of the complex number $\tilde{B}(k_y)$. Therefore, the estimated kernel that we can extract from our simulation is of the form

$$\begin{aligned}\tilde{\eta}^a(k_y) &\equiv -\frac{\tilde{P}^a_{yx}(k_y)}{\tilde{\dot{\gamma}}(k_y)} \\ &= -\left[\frac{\tilde{P}_{yx}(k_y)}{\tilde{\dot{\gamma}}(k_y)} - \frac{\tilde{P}^e_{yx}(k_y)}{\tilde{\dot{\gamma}}(k_y)}\right] \\ &= \tilde{\eta}(k_y) - \frac{2\mathrm{i}|\tilde{B}(k_y)| \sin(k_y a + \phi_{k_y})}{\tilde{\dot{\gamma}}(k_y)}.\end{aligned} \tag{10}$$

The last term in equation (10) represents the error that results from the restriction of the domain of $P_{yx}(y)$. If the strain rate has zeros that are not exactly cancelled by zeros in the numerator then it is possible for the error term to diverge at certain values of k_y. For example, if the strain rate is given by the ramp function

$$\dot{\gamma}(y) = -\alpha\, \Pi_a(y)\, y, \tag{11}$$

where α is a positive constant then its Fourier transform is

$$\tilde{\dot{\gamma}}(k_y) = -2\mathrm{i}\alpha \left[\frac{k_y a \cos(k_y a) - \sin(k_y a)}{k_y^2} \right], \tag{12}$$

which has zeros at points $k_y a = z_n$ where z_n are the roots of the equation $\tan(z) = z$. In general, these zeros may not be cancelled by the corresponding zeros in the numerator of the error term, implying that divergences in $\tilde{\eta}^a(k_y)$ are to be expected.

2.3. Explicit example

For the purposes of illustration only we approximate the viscosity kernel by an exponentially decaying function in order to keep the mathematical analysis relatively simple, though the exact functional form is not yet settled [11, 13]. Recent work suggests that the k-space kernel has a shape more akin to a combination of Gaussians or a Lorentzian [14]. The mathematical simplification of a decaying exponential does not however affect the general conclusions we will reach, which is the goal of the present work. Let us therefore consider a test case example to illustrate the ideas generated in the previous section by assuming that the strain rate is given by equation (11) (i.e., no significant layering of fluid near the walls) and the viscosity kernel is given by

$$\eta(y) = \frac{\eta_0}{2\xi} \mathrm{e}^{-\frac{|y|}{\xi}}, \tag{13}$$

which has the Fourier transform

$$\tilde{\eta}(k_y) = \frac{\eta_0}{1 + (k_y \xi)^2}. \tag{14}$$

The profiles of $\eta(y)$ and $\tilde{\eta}(k_y)$ for this idealized fluid are shown in figure 2. One can compute the exact shear stress either by computing the k-space stress as $\tilde{P}_{yx}(k_y) = -\tilde{\eta}(k_y)\,\tilde{\dot{\gamma}}(k_y)$ and taking the inverse transform, or directly by applying the convolution via equation (3). In either case we find

$$P_{yx}(y) = \frac{\alpha \eta_0 \xi}{2} \begin{cases} \left[\left(1 - \dfrac{a}{\xi}\right) \mathrm{e}^{\frac{(y+a)}{\xi}} - \left(1 + \dfrac{a}{\xi}\right) \mathrm{e}^{\frac{(y-a)}{\xi}} \right]; & y < -a \\ 2\dfrac{y}{\xi} + \left(1 + \dfrac{a}{\xi}\right) (\mathrm{e}^{-\frac{(y+a)}{\xi}} - \mathrm{e}^{\frac{(y-a)}{\xi}}); & -a < y < a \\ -\left[\left(1 - \dfrac{a}{\xi}\right) \mathrm{e}^{-\frac{(y-a)}{\xi}} - \left(1 + \dfrac{a}{\xi}\right) \mathrm{e}^{-\frac{(y+a)}{\xi}} \right]; & a < y. \end{cases} \tag{15}$$

Clearly the support of $P_{yx}(y)$ extends beyond the support of $\dot{\gamma}$, i.e. beyond the fluid–wall interface. Figure 3 demonstrates this diagrammatically. Restricting the domain of $P_{yx}(y)$ to $(-a, a)$ clearly results in a significant loss of information that is required to fully reconstruct the kernel given by equation (13) if the de-convolution method is applied to equation (3).

We now proceed to quantitatively analyse the extent to which this loss of information affects the shape of the estimated kernel. In the case of our test example, the function $b(y)$ is

$$b(y) = \frac{\alpha\, \eta_0\, \xi}{2} \left[\left(\frac{a}{\xi} - 1 \right) + \left(\frac{a}{\xi} + 1 \right) \mathrm{e}^{-\frac{2a}{\xi}} \right] \Theta(y)\, \mathrm{e}^{-\frac{y}{\xi}}, \tag{16}$$

where $\Theta(y)$ is the Heaviside step function. This has the Fourier transform

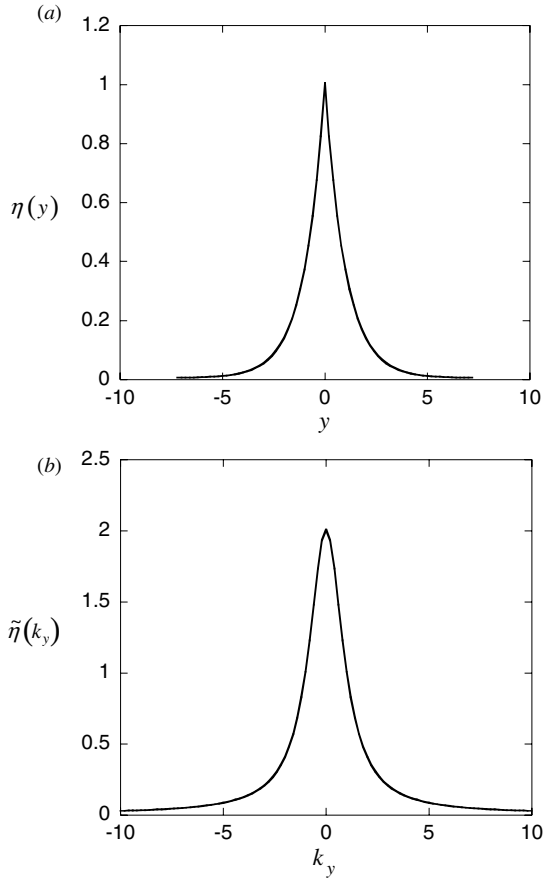

Figure 2. (*a*) Non-local viscosity kernel for our test example defined by equation (13). (*b*) Fourier transform of test viscosity kernel as given by equation (14). In both (*a*) and (*b*) we set $\eta_0 = 2,\ \xi = 1$ for illustrative purposes.

$$\tilde{B}(k_y) = \frac{\alpha\,\eta_0\,\xi}{2}\left[\left(\frac{a}{\xi} - 1\right) + \left(\frac{a}{\xi} + 1\right)\mathrm{e}^{-\frac{2a}{\xi}}\right]\frac{\xi}{1 + \mathrm{i}\,k_y\xi}. \tag{17}$$

Our idealized strain rate profile given by equation (11) has the Fourier transform given by equation (12). Thus, substitution of equations (12), (14) and (17) into equation (10) gives for the estimated transformed kernel

$$\tilde{\eta}^a(k_y) \equiv \frac{\eta_0}{1 + (k_y\xi)^2}\left\{1 + \left|\left(\frac{a}{\xi} - 1\right) + \left(\frac{a}{\xi} + 1\right)\mathrm{e}^{-\frac{2a}{\xi}}\right|\frac{\xi^2 k_y^2(\sin(k_y a - \arctan(k_y\xi)))}{2(k_y a\cos(k_y a) - \sin(k_y a))}\right\}. \tag{18}$$

Comparison of equation (18) for the estimated kernel which results from the use of a stress that is restricted to the domain of the strain rate $(-a, a)$ with the exact kernel given by equation (14) shows that significant error is introduced by domain restriction. In particular, equation (18) shows that domain restriction results in divergences in the Fourier transform of the viscosity kernel at a sequence of values of $k_y a$, the first such divergence occurs at $k_y a \approx 4.5$. This is

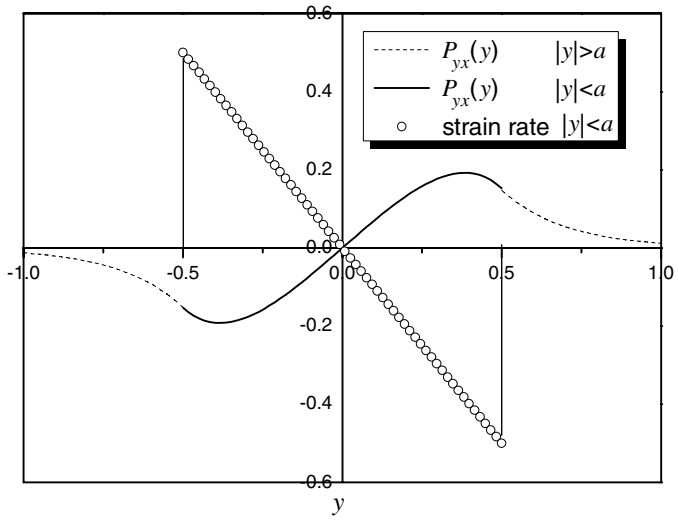

Figure 3. Strain rate given by equation (11) for our ramp-like test function (hollow circles) and resulting shear stress computed by equation (15). For illustrative purposes we choose $a = 0.5$, $\eta_0 = 1$ and $\xi = 0.2$.

shown in figure 4, in which the exact and estimated k-space kernels are plotted for comparison purposes.

With this in mind we now also compute discrete Fourier transforms (DFTs) of our estimated kernels for our simple test system. Our objective here is to observe any qualitative differences between the known analytic true kernel and the DFT of the estimated kernel and to relate these to the DFT kernels obtained for our simulated molecular dynamics systems in section 3. Interested readers may also refer to appendix B for a more detailed discussion on the DFTs. In figure 5 we show a comparison of the true analytic viscosity kernels (r-space and k-space) defined by equations (13) and (14) respectively with estimated kernels computed by the DFT method. In figure 5(a) the k-space kernel is computed via equation (4) where the true support of $P_{yx}(y)$ is used and the strain rate data are padded with zeros up to $\sqrt{5}$ times the length of its own support, i.e. $\sqrt{5}a$. The agreement between the exact and DFT kernels is excellent. Similarly, in figure 5(b) the true kernel in r-space is plotted alongside the estimated kernel which is computed by taking the inverse DFT of the estimated k-space kernel in figure 5(a). Again excellent agreement is found. This demonstrates clearly that when the true support of the shear stress is used one can be confident that the estimated kernel computed by the DFT is in very good agreement with the true kernel. If we now restrict the support of the stress such that it is equal to the support of the strain rate (i.e., in the domain $(-a, a)$ with no padding) a very different result is obtained in figure 6. In this case we see that the estimated k-space kernel (figure 6(a)) is broader than the true kernel. Furthermore, instead of decaying to zero as $k_y \to \infty$ we find that the kernel is vertically shifted and sits on a constant background. If we perform the inverse DFT on the estimated kernel we now find that in r-space the estimated kernel seems to underestimate the area of the kernel.

Clearly the use of the DFT in conjunction with the restricted support of the shear stress results in a k-space viscosity kernel that does not decay to zero. The reason for this will be discussed in the next section (see also appendix B). For the moment we note that this has an

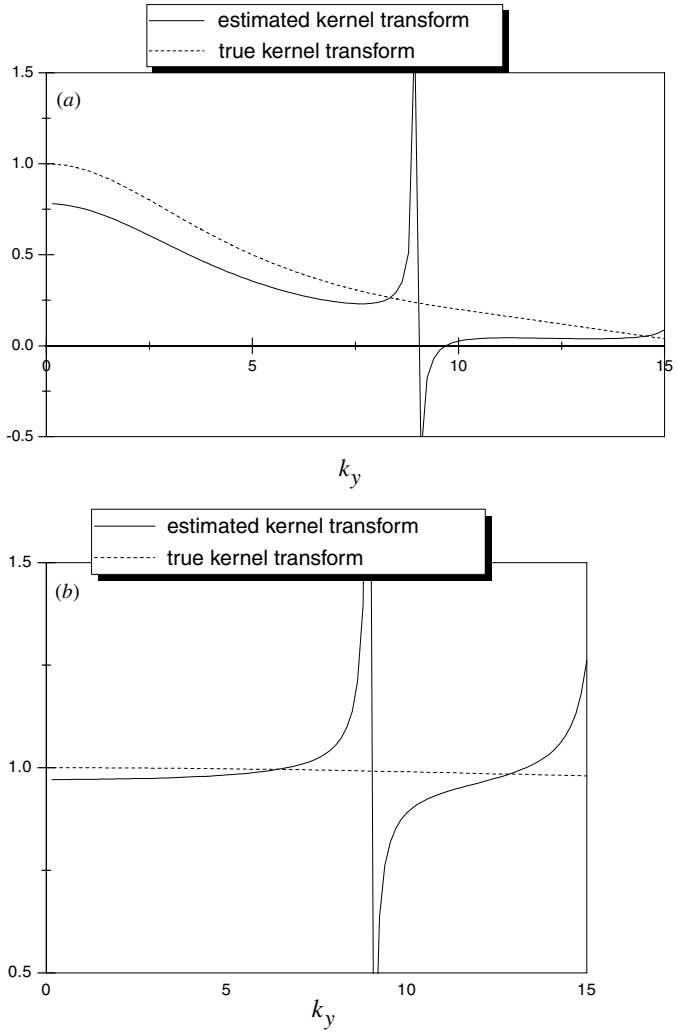

Figure 4. (*a*) Comparison of the true kernel transform $\tilde{\eta}(k_y)$ (dashed line, via equation (14)) with the estimated kernel transform $\tilde{\eta}^a(k_y)$ (solid line, via equation (18)) based on restricted domain data. $a = 0.5$, $\eta_0 = 1$ and $\xi = 0.2$. (*b*) As with (*a*) but with smaller effective length scale of the kernel, $\xi = 0.01$.

important consequence for the real-space viscosity kernel. Let the estimated k-space kernel be shifted by a constant non-zero value K such that

$$\tilde{\eta}^a(k_y) \sim \tilde{\eta}(k_y) + K. \tag{19}$$

Taking the inverse transform gives

$$\eta^a(y) \sim \eta(y) + K\delta(y), \tag{20}$$

where $\delta(y)$ is the Dirac delta function. Thus, a non-decaying estimated kernel in k-space results in a delta function which will appear as a spike at the origin in the DFT inverse transforms. For the purposes of display, this spike has been removed from the $y = 0$ point in figure 6(*b*).

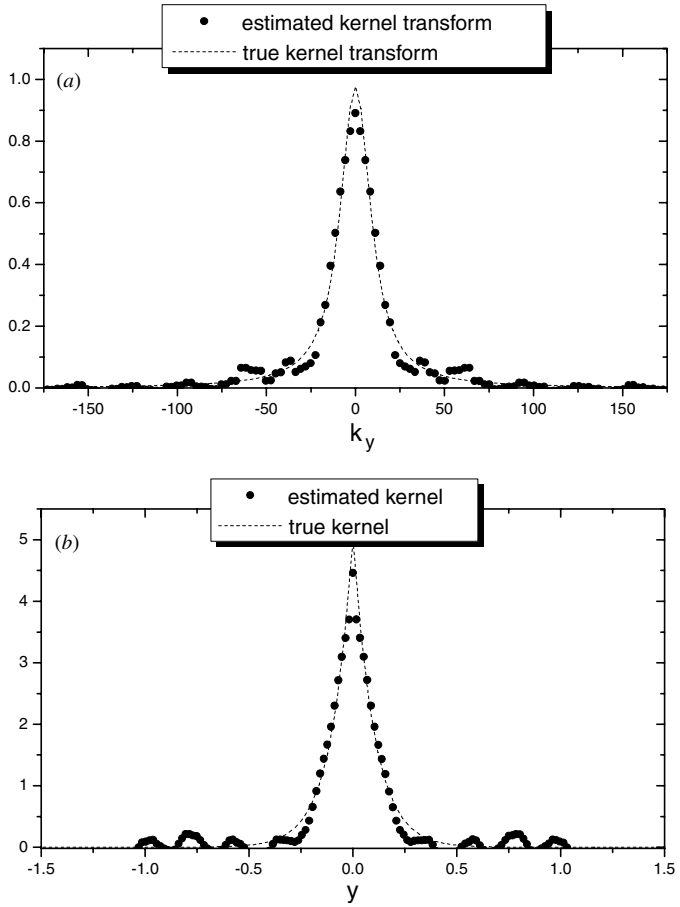

Figure 5. (*a*) Comparison of the true kernel transform $\tilde{\eta}(k_y)$ (dashed line via equation (14)) with the estimated kernel transform $\tilde{\eta}^a(k_y) \equiv -\tilde{P}_{yx}(k_y)/\tilde{\dot{\gamma}}(k_y)$ by the DFT method (filled dots). Exact values and the true support of $P_{yx}(y)$ with padding to $\sqrt{5}$ times the length of the support of $\dot{\gamma}(y)$ are used. (*b*) Comparison of the true kernel $\eta(y)$ (dashed line via equation (13)) with the estimated kernel $\eta^a(y)$ (filled dots) by inverse DFT of $\tilde{\eta}^a(k_y)$ shown in (*a*). $a = 0.5$, $\eta_0 = 1$ and $\xi = 0.1$.

However, these spikes are clearly observed in the real-space kernels of our simulation data, and this will be discussed further in section 3.

What is clear to us now is that the shapes of the estimated viscosity kernels in *k*-space and *r*-space obtained by the use of DFTs on a restricted data set are distorted such that the *k*-space kernels do not decay to zero as they should and, as a consequence, the *r*-space kernels are suppressed in magnitude and have an unphysical spike at $y = 0$. Nevertheless, their overall shape appears to remain qualitatively similar to their true shape.

3. Nonequilibrium molecular dynamics simulations: comparison with mathematical model

3.1. Simulation parameters

Our simulation geometry is displayed in figure 1. All atoms interact via a truncated and shifted Lennard–Jones potential (the Weeks–Chandler–Andersen potential [15]), and wall atoms are

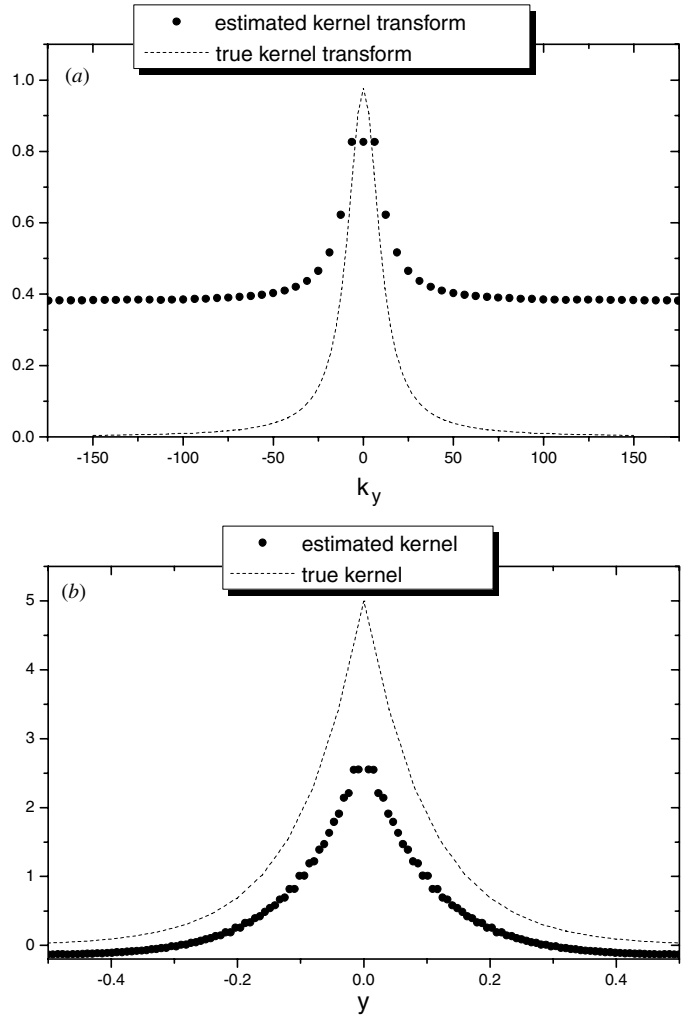

Figure 6. As for figure 5, but the data were sampled only over the support of $\dot{\gamma}(y)$ and processed without padding. Note the elevated floor in the estimated kernel transform. The value of $\tilde{\eta}^a(k_y = 0)$ is taken as the average of the two adjacent points. We do not plot the delta-function spike at $\eta^a(y = 0)$ for display purposes.

additionally tethered to their equilibrium sites by a harmonic potential. So as not to weigh down the present paper with technical details of the simulation system, we refer readers to [1, 12, 16], in which full details of the geometry and algorithms used are given. We briefly summarize as follows.

The slit-pore model consists of a single wall comprising three layers of atoms arranged in an FCC lattice, which are allowed to vibrate. Periodic boundary conditions were applied in all three Cartesian directions so that only one wall is needed per simulation cell to represent a slit pore. Simulations were conducted at three different reduced pore widths: $L/\sigma = 5.1$, 10.2 and 15.3, where the pore width, L, is defined as the distance between the centres-of-mass of the two innermost opposing wall layers (throughout the remainder of this paper

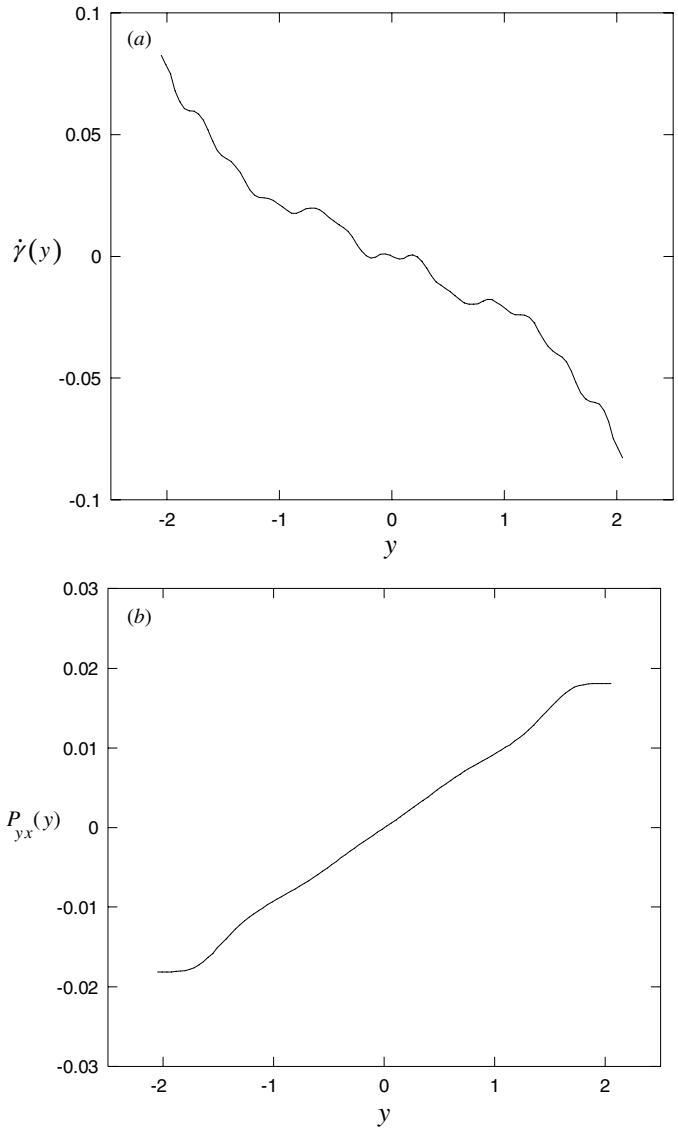

Figure 7. P_{xy} and $(\dot{\gamma})$ as functions of y for average fluid densities of $\rho = 0.442$ and channel width $L = 5.1$.

all quantities are given in reduced units defined in terms of the LJ energy and distance parameters).

A constant force (pressure head) in the positive x-direction is applied to all fluid atoms to generate our flow (the equivalence of Poiseuille flow and gravity driven flow for molecular simulations has been explained previously [12]). The magnitude of the pressure head used in this work was $F_e = 0.02$ in reduced dimensionless units for all systems studied. This value was chosen to maximize the signal-to-noise ratio while maintaining a linear response. In all our simulations, the number of wall atoms was fixed at 216 (72 atoms per layer). The number

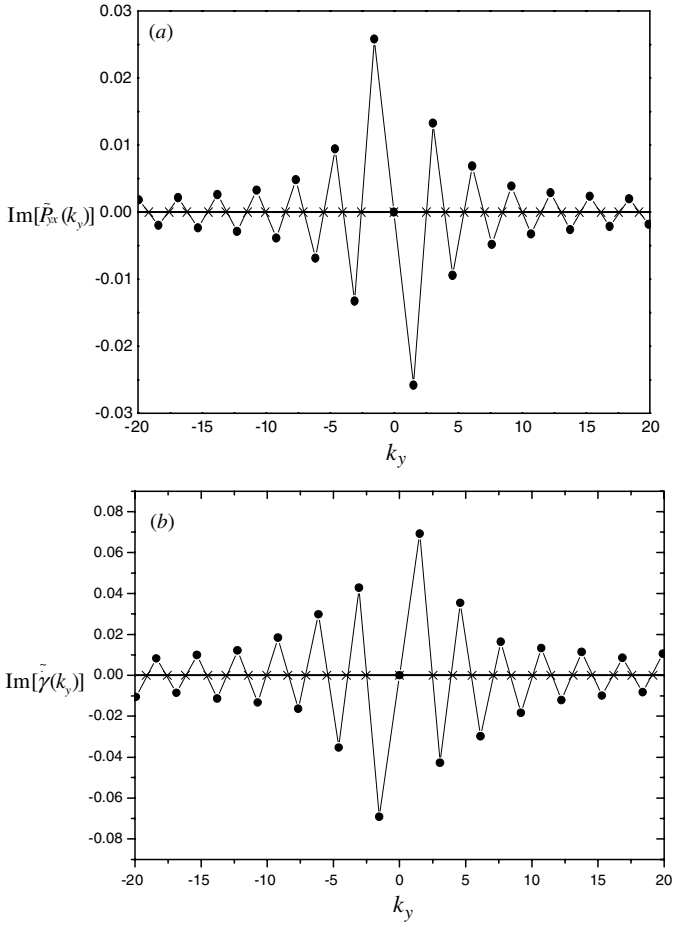

Figure 8. (*a*) Imaginary part of the transformed shear stress in figure 2; (*b*) imaginary part of the transformed strain rate in figure 2. Filled dots represent actual DFT data, while crosses depict approximate zeros.

of fluid atoms differed, depending on the value of the pore width: 216, 504 and 864 for $L = 5.1$, 10.2 and 15.3 respectively. For each pore width we simulated fluid densities equal to 0.442 and 0.650, with a constant wall density for all systems of 0.850. We note that the number of particles does not scale in the same proportion as the width since the lengths of the simulation box in the x and z directions differ for each system size studied in order to maintain the same densities.

The equations of motion for the wall and fluid atoms were integrated using a fifth-order Gear algorithm with a time step of 0.001. A Gaussian thermostat was applied to the wall atoms to maintain a constant wall temperature of 0.722 throughout the simulations. No thermostats are applied to the fluid and the viscous heat generated is allowed to dissipate via conduction through the walls.

Our simulations were first equilibrated to a steady state before accumulation of data. Production runs were then conducted for a duration of 400 million time steps. The shear stress was computed by integrating the momentum continuity equation [12], and the streaming velocity and density were collected in bins of small width.

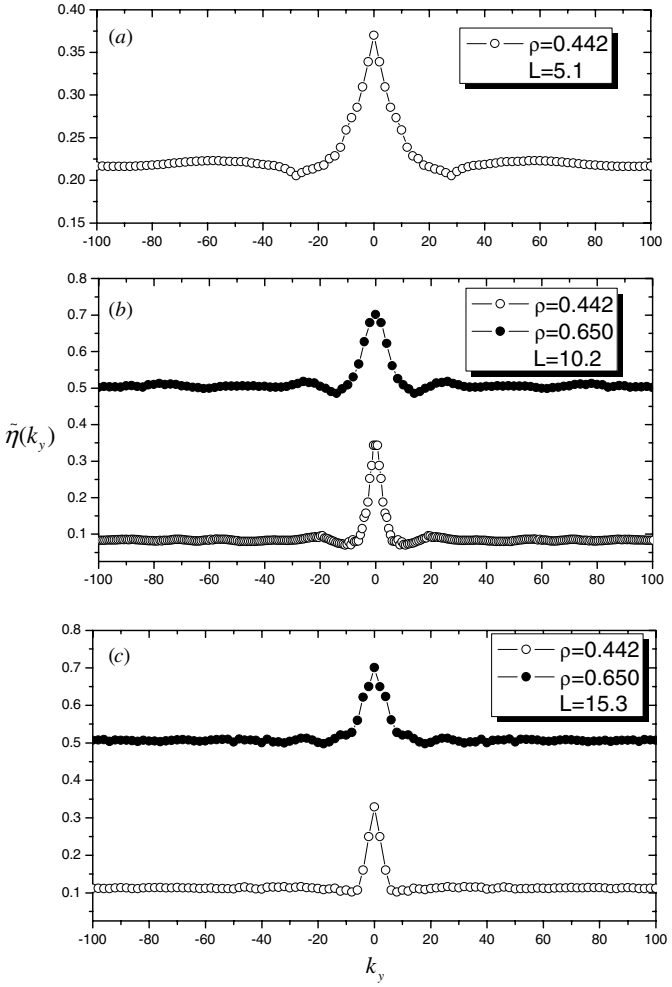

Figure 9. *k*-space non-local viscosity kernels for average fluid densities of $\rho = 0.442$ and 0.650. (*a*) $L = 5.1$; (*b*) $L = 10.2$; (*c*) $L = 15.3$.

3.2. Simulation results

As an example of what the strain rate and stress profiles look like, in figure 7 we plot $\dot{\gamma}$ and P_{yx} as functions of position in the channel. The fluid density is 0.442 and the fluid is confined to a narrow channel of length $L = 5.1$. The strain rate is computed by accumulating the velocity profile in bins of width 0.0414 and numerically differentiating with respect to y. In figure 8 we show what the discrete Fourier transformed (DFT) stress and strain rate profiles of figure 7 look like (see appendix B for details on the DFT methodology). In all discrete Fourier transforms and inverse transforms performed in this work the number of sampling points is chosen to be optimal and is generally $\geqslant$100 (see 16] for specific details). The numerical recipe for judiciously choosing the sampling period and number of sampling points may be found in any standard text on numerical Fourier transforms. Only the imaginary components are non-zero and contribute to the viscosity kernel. In figure 9 we plot the Fourier-transformed

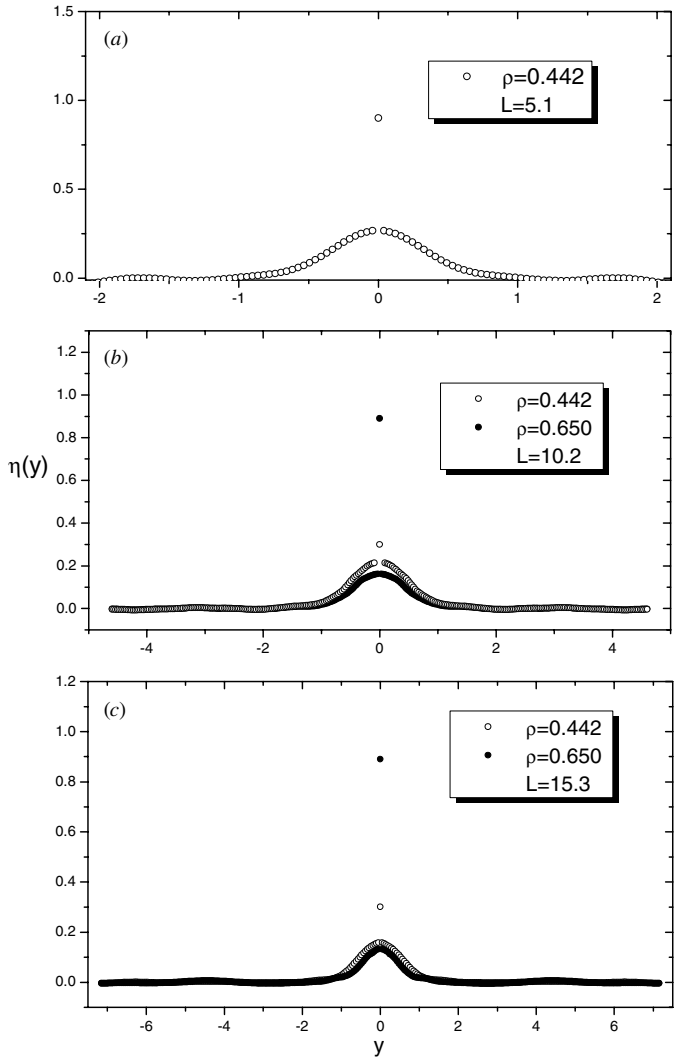

Figure 10. Real-space non-local viscosity kernels for average fluid densities of $\rho = 0.442$ and 0.650. (*a*) $L = 5.1$; (*b*) $L = 10.2$; (*c*) $L = 15.3$.

(*k*-space) viscosity kernels for systems of various channel widths and fluid densities (obtained via equation (4)), while in figure 10 we plot the kernels in real space. The argument y of the kernel must be interpreted as a *relative* separation between two points in space (see the second part of [1]). There are several important features of these plots that we now discuss and relate back to our mathematical model presented in the preceding sections.

First, the *k*-space kernels have a maximum at $k_y = 0$ (the infinite wavelength viscosity which is approximately equal to the Navier–Stokes viscosity defined in 1) , which then decays as k_y increases. However $\tilde{\eta}(k_y)$ does not decay to zero as one might expect but rather decays to a constant value, though this trend is more pronounced for higher density fluids and narrower channel widths. This in fact is exactly what we observe in our mathematical model, as explained in detail in the previous section (see also appendix B).

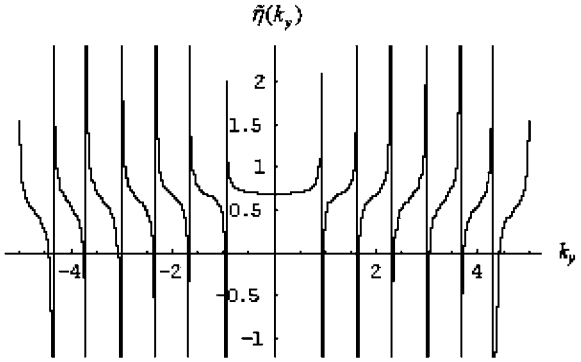

Figure 11. $\tilde{\eta}(k_y) \equiv -\tilde{P}_{yx}(k_y)/\tilde{\dot{\gamma}}(k_y)$ for the system $\rho = 0.650$, $L = 10.2$, where the transformed shear stress and strain rate are computed analytically.

Second, the real-space kernels have maxima at $y = 0$ and decay to zero within several effective atomic diameters length. Thus, equation (3) tells us that the contribution to the fluid's shear stress at any point is greatest in the immediate vicinity of that point and becomes almost exponentially less important as the distance from that point increases. The shapes of our simulation kernels are thus qualitatively similar to the kernels we have used in our mathematical modelling. Furthermore $\eta(y)$ has a spike at $y = 0$ that is not physically meaningful (note that the data have not been filtered). As previously noted from our mathematical model, this spike is a consequence of a k-space kernel that does not decay to zero, but rather is superposed on a constant background; inverse transforming results in a delta-function spike at $y = 0$. Furthermore, it is identically true that $\eta(y = 0) = \frac{1}{2\pi}\int_{-\infty}^{\infty} \mathrm{d}k_y\, \tilde{\eta}(k_y)$, and this is indeed the case as displayed by the simulation data. Similarly it is required that $\tilde{\eta}(k_y = 0) = \int_{-\infty}^{\infty} \mathrm{d}y\, \eta(y)$. However, the spike at $\eta(y = 0)$ demands that the profile of $\eta(y)$ is altered such that this condition is mathematically obeyed. Thus, the shape of the kernel in real space may not be its true shape. In fact this can be clearly observed by noting that, apart from the spike at $\eta(y = 0)$, the values of $\eta(y)$ for the denser fluids in figures 10(b) and (c) are actually *lower* than those for the less dense fluid, something which is physically not possible (the viscosity of a less dense fluid is always less than that of an identical fluid at a higher density at the same temperature and volume). In terms of our mathematical model, this is equivalent to saying $\tilde{\eta}^a(k_y = 0) = \int_{-\infty}^{\infty} \mathrm{d}y\, \eta^a(y)$. Therefore, if a spike exists at $y = 0$ the inverse DFT will suppress all subsequent values of $\eta^a(y)$ such that the overall integral of $\eta^a(y)$ is equal to $\tilde{\eta}^a(k_y = 0)$. This then explains why, apart from the value $\eta^a(y = 0)$, $\eta^a(y)$ is lower than the true kernel for most (if not all) other values of y. This also explains why, apart from the spike at $\eta^a(y = 0)$, the values of $\eta^a(y)$ for the denser fluids in figures 10(b) and (c) are actually *lower* than those for the less dense fluid. This is of course physically unsound and is a consequence only of a mathematical formalism that necessarily couples the Fourier transform to its inverse. These results are again completely consistent with our mathematical modelling of the preceding two sections. We also find that the k- and r-space kernels approach the true kernel for systems of a relatively large pore width compared to the width of the kernel as well as for lower density fluids. This is consistent with our expectations, as discussed in both the introduction and section 2.

Finally, by fitting the shear stress and strain rate profiles by analytic series functions and taking the ratio of the analytic Fourier transforms of these quantities one finds that the transformed viscosity kernels have singularities at regular intervals of k_y. This is displayed

in figure 11, in which we plot $\tilde{\eta}^a(k_y)$ for our simulated molecular dynamics system of $\rho = 0.65$, $L = 10.2$. In this case we do not take DFTs of our stress and strain rate profiles, but rather fit simple series functions to them (see [4, 16]). The Fourier transforms are then performed analytically and the ratio of them are taken to obtain what is essentially $\tilde{\eta}^a(k_y)$ for our simulated system. Note the divergences that occur at values of $k_y \approx 0.69n$, where n are integers. These divergences are similar to what we have computed in our mathematical model as displayed in figure 4 and are a direct consequence of not knowing what the full stress response function is in order to accurately extract the true viscosity kernel. These divergences can be avoided in the discrete Fourier transforms if one samples the data such that zeros in the transformed strain rate are not sampled (e.g., see figure 8(*b*)).

4. Conclusions

We have performed a critical analysis of the validity of using a simple linear hydrodynamic constitutive equation to compute the non-local shear viscosity for confined fluids. The model, which currently assumes a homogeneous (effective) viscosity kernel, is reasonable for relatively wide pores and low density fluids but is seen to be limited in accuracy for the case of high densities and narrow confinement. We have analysed the model to determine the origin of the sources of error and found that a combination of domain restriction and the circular convolution (see appendix B) inherent in the discrete Fourier transform methodology leads to (a) singularities in the estimated kernel, and (b) a non-zero tail in the k-space kernel for large k, which manifests itself as a delta-function spike at $y = 0$ for the r-space kernel. While it is possible to avoid the problems in (a) by suitable sampling of points that avoid these singularities, (b) leads to a distortion of the shape of the true kernel, which is not easily corrected.

In addition to the efforts described above, though not described in any detail in this paper, we also attempted to perform direct inversions to extract the kernel, without attempting to Fourier transform the available data. This can be achieved by discretizing equation (3) and selecting only those values that contribute to the shape of the kernel. This leads to a set of linear equations, which can be solved to extract the kernel. Furthermore, noise reduction can be achieved by least-squares methods to minimize the error in the calculated stress. Both methods yield kernels that are reasonable away from the centre of the pore, but still give a spike at $y = 0$. To try to remove this spike we then attempted a truncated singular value decomposition (SVD) on the data. While this did indeed remove the spike at $y = 0$ this was at the cost of introducing some small artefacts at the limits of the sampled range. The procedure seems to work reasonably well for the low density systems, but not so well for small pores and high densities. Furthermore, there is no clearly defined way for setting the number of terms to include in the SVD.

While it may be possible to remove the finite non-zero component of the k-space kernel by computing Fourier coefficients of the kernel, or even obtain reasonable kernels for low density systems via direct inversion, the fundamental theoretical challenge that remains is to include the position dependence into the kernel so that it becomes a genuinely inhomogeneous function of space and also to appropriately model the boundary conditions at the fluid–wall interface, including stick/slip boundary conditions. The foregoing discussion makes it clear that a constitutive equation more general than equation (3) is required if we are to successfully describe non-local viscosity effects in a confined fluid. Equation (2) suggests that a more general constitutive equation that uses the idea of a non-local viscosity kernel to describe steady planar shear would have the following form:

$$P_{yx}(y) = -\int_{-\infty}^{\infty} \eta(y, y - y')\dot{\gamma}(y')\,\mathrm{d}y'. \tag{21}$$

We have already seen that if we assume that the viscosity kernel is independent of y (translationally invariant) for a confined fluid, the restricted domain of the strain rate is not sufficient to reproduce the observed stress behaviour. Therefore, we are forced to abandon the idea of a y-independent viscosity kernel to describe non-local viscosity effects in a confined fluid. The next simplest viscosity kernel that would incorporate the non-local viscosity effects and account for the y-dependence of the fluid response in a confined fluid would be given by

$$\eta_c(y, y - y') = W_a(y)\eta(y - y'), \tag{22}$$

where $W_a(y)$ is a function that provides information about the position dependence of the kernel, η_c represents the confined fluid viscosity kernel and η represents the (translationally invariant) viscosity kernel for an unconfined (infinite) fluid at the same thermodynamic state.

For the purposes of illustration only, consider the case where $W_a(y) = \Pi_a(y)$, and $\Pi_a(y)$ is the top-hat function defined previously (equation (6)). We now see that, whereas η is a material property that could be determined independently, η_c is an explicitly y-dependent function that depends on the geometry of the confinement. It is readily seen that this simple modification not only makes it possible to reproduce the observed shear stress profile, it also shows that the extraction of the non-local viscosity kernel using equation (4) is doomed to failure, because the viscosity kernel can no longer be extracted by Fourier transformation of a simple convolution. Instead, we must take the Fourier transform of a product of two functions of y, which then becomes a convolution in k-space. For a highly confined fluid undergoing any type of flow, the spatial truncation of the stress response makes it impossible to accurately extract the non-local viscosity kernel, as we have shown in the preceding sections. However, it should still be possible to predict the stress profile, given a strain rate profile and an independently determined non-local position-dependent viscosity kernel. Such a kernel could be computed either via transverse momentum autocorrelation functions [3, 14] of an equilibrium fluid at equivalent thermodynamic state points that correspond to those in a confined fluid, or the sinusoidal transverse field (STF) method [14, 17, 18], again at equivalent state points. This procedure would completely eradicate the problems experienced in trying to extract the viscosity kernel directly from a set of confined fluid data. It would additionally allow us to predict the flow velocity profile, given the knowledge of the shear stress. This is the approach that we are currently undertaking [14]. Indeed, we have shown [19] that this method is able to accurately predict the shear stress for a homogeneous fluid under the influence of a weak sinusoidal force in which the rate of strain varies appreciably over the width of the kernel. The local constitutive model (Newton's law of viscosity) completely breaks down in this regime.

Acknowledgments

JZ thanks the Australian government for financial assistance. We also thank Professor Denis Evans for helpful discussions.

Appendix A

Let the shear stress be defined by equation (3) and the strain rate as in equation (11). Now, let the kernel have support of order ξ. Therefore, the full support of the stress is of order

$-a-\xi \leqslant y \leqslant a+\xi$. We can write equation (3) as

$$\begin{aligned} P_{yx}(y) &= -\int_{-\infty}^{\infty} \mathrm{d}y'\, \eta(y-y')\, \dot{\gamma}(y') \\ &= -\left[\int_{-\infty}^{-a} \mathrm{d}y'\, \eta(y-y')\, \dot{\gamma}(y') + \int_{-a}^{a} \mathrm{d}y' \eta(y-y')\dot{\gamma}(y') + \int_{a}^{\infty} \mathrm{d}y'\, \eta(y-y')\dot{\gamma}(y')\right]. \end{aligned} \tag{A.1}$$

Since the strain rate is a ramp function defined to be non-zero only in the range $(-a, a)$, the first and last terms in equation (A.1) are zero. The second term can be rewritten as

$$\begin{aligned} \int_{-a}^{a} \mathrm{d}y'\, \eta(y-y')\, \dot{\gamma}(y') &= -\alpha \int_{-a}^{a} \mathrm{d}y'\, \eta(y-y')\, y' \\ &= -\alpha \int_{y-a}^{y+a} \mathrm{d}s\, \eta(s)\, (y-s), \end{aligned} \tag{A.2}$$

where we have used the substitution $s = y - y'$. Substituting equation (A.2) into equation (A.1) gives

$$\begin{aligned} P_{yx}(y) &= \alpha y \int_{y-a}^{y+a} \mathrm{d}s\, \eta(s) - \alpha \int_{y-a}^{y+a} \mathrm{d}s\, \eta(s)\, s \\ &= \alpha y \left[\int_{y-a}^{-a} \mathrm{d}s\, \eta(s) + \int_{-a}^{a} \mathrm{d}s\, \eta(s) + \int_{a}^{y+a} \mathrm{d}s\, \eta(s)\right] - \alpha \int_{y-a}^{y+a} \mathrm{d}s\, \eta(s)\, s. \end{aligned} \tag{A.3}$$

The second term in square brackets is just the integral of the kernel and is a constant equal to the effective infinite wavelength viscosity, defined here as $\tilde{\eta}(k=0) \equiv \eta_0$. Therefore,

$$P_{yx}(y) = \alpha\eta_0 y + \alpha y \left[\int_{y-a}^{-a} \mathrm{d}s\, \eta(s) + \int_{a}^{y+a} \mathrm{d}s\, \eta(s)\right] - \alpha \int_{y-a}^{y+a} \mathrm{d}s\, \eta(s)\, s. \tag{A.4}$$

This expression says that the stress is a linear function of position plus some nonlinear terms that are important only in the regions near the walls. This is seen to be the case, as observed in figure 7. If there were no walls, the stress would simply be a linear function of y (i.e., the convolution of an infinite ramp is another infinite ramp whose slope is given by the integral of the kernel). As ξ increases in range, the nonlinear profile of the shear stress also increases in extent and becomes more prominent.

Appendix B. Discrete Fourier transforms (DFTs)

The main potential problem with the use of DFTs for a domain-restricted set of data such as ours is that the true convolution implicit in equation (3) may not be well approximated by the circular convolution that is implicit in the DFT. The DFT assumes that the data set is periodic in space such that if $\tilde{F}^T(k_y)$ is the true Fourier transform of some function $f(y)$, then it is approximated by the DFT ($\tilde{F}(k_y)$) by [20]

$$\begin{aligned} &\tilde{F}^T(k_y) \approx \tilde{F}(k_y); \qquad 0 \leqslant k_y \leqslant \pi/T \\ &\tilde{F}^T(k_y) \approx \tilde{F}(k_y) = \tilde{F}\left(k_y + \frac{2\pi}{T}\right); \qquad -\pi/T \leqslant k_y \leqslant 0, \end{aligned} \tag{B.1}$$

where T is the sampling period and the system is periodic with period $2\pi/T$ over the interval $(-\pi/T, \pi/T)$. Thus, when using a DFT the linear convolution represented by equation (3) is replaced by a circular convolution, which is defined as follows.

If equation (3) is discretized it may be written as

$$P_{yx}[n] = -\sum_{i=-\infty}^{\infty} \eta[n-i]\, \dot{\gamma}[i]. \tag{B.2}$$

Typically in applications that involve DFTs the impulse response function (what we call the kernel function) has a finite response, which implies that $\eta[n]$ is of finite length. It is common to define $\eta[n]$ on the interval $0 \leqslant n \leqslant N-1$, where N is the number of sampling points. In this case the DFT is defined in the standard way, i.e. as a one-sided transform ranging from 0 to $N-1$ instead of $-N/2$ to $N/2$ as is the case for the two-sided transform. It is a standard practice in DFT use to draw on the symmetry property that links the one-sided and two-sided transforms together. The two-sided transform can be written as a one-sided transform simply by invoking the periodicity inherent via equation (B.1) (see the second part of [1] for an explicit example). Usually the data set $\dot{\gamma}[n]$ is also of finite length, which implies that $P_{yx}[n]$ is also.

Consider two sequences $\dot{\gamma}[n]$ and $\eta[n]$, of lengths M and N, respectively, and defined for positive values of n only. Equation (B.2) then reduces to the following finite summation (where here we work with the one-sided convolution to illustrate the ideas):

$$P_{yx}[n] = -\sum_{i=0}^{M-1} \eta[n-i]\,\dot{\gamma}[i] = -\sum_{i=0}^{N-1} \eta[i]\,\dot{\gamma}[n-i]; \qquad 0 \leqslant n < M+N-1. \tag{B.3}$$

This output function has a length $M+N-1$ and is known as a linear convolution.

Now consider the case where $M=N$ and the functions are periodic, i.e., $\eta[n] = \eta[n+N]$ and $\dot{\gamma}[n] = \dot{\gamma}[n+N]$. The output function is also periodic with length N and can be computed as

$$P_{yx}[n] = -\sum_{i=0}^{N-1} \eta[(n-i)_N]\,\dot{\gamma}[i] = -\sum_{i=0}^{N-1} \eta[i]\,\dot{\gamma}[(n-i)_N]; \qquad 0 \leqslant n < N-1, \tag{B.4}$$

where the notation $(n-i)_N$ is defined as $\mathrm{Mod}(n-i, N)$ [21]. This is known as circular convolution and is implicit in any finite range DFT. All our convolutions are thus circular in nature and our DFTs are periodic over the range of our data set.

We now note that there are two potential problems that can arise out of using the DFT with data processed without padding. The first is the replacement of the linear convolution in equation (3) by a circular convolution. The second is aliasing errors due to inadequate sampling rates. In what follows we will show that the combination of a ramp-like strain rate and the implicit circular convolution inherent in the DFT is sufficient to account for the observation that $\tilde{\eta}(k_y)$ does not decay to zero as $k_y \to \infty$ but rather sits on a constant value. Recall that this is what causes the delta-function spike at $y=0$ in the real-space kernel, which in turn suppresses all subsequent values of $\eta(y)$ resulting in a narrower estimated kernel.

We pose the question: what is the relationship between the kernel reproducing the observed data assuming a circular convolution and the true linear convolution kernel? To help answer this question we first define a periodic function

$$r(y) = R(y) * \sum_{n=-\infty}^{\infty} \delta(y - n2a), \tag{B.5}$$

where $R(y)$ is an input ramp-like function with support $-a \leqslant y < a$. The linear convolution of R with the kernel is given as

$$\begin{aligned} \sigma(y) = \eta(y) * R &= \int_{-\infty}^{\infty} \eta(y-y')R(y')\,\mathrm{d}y' \\ &= \sigma_R(y) = \int_{-a}^{a} \eta(y-y')R(y')\,\mathrm{d}y'\,; \qquad -a \leqslant y < a. \end{aligned} \tag{B.6}$$

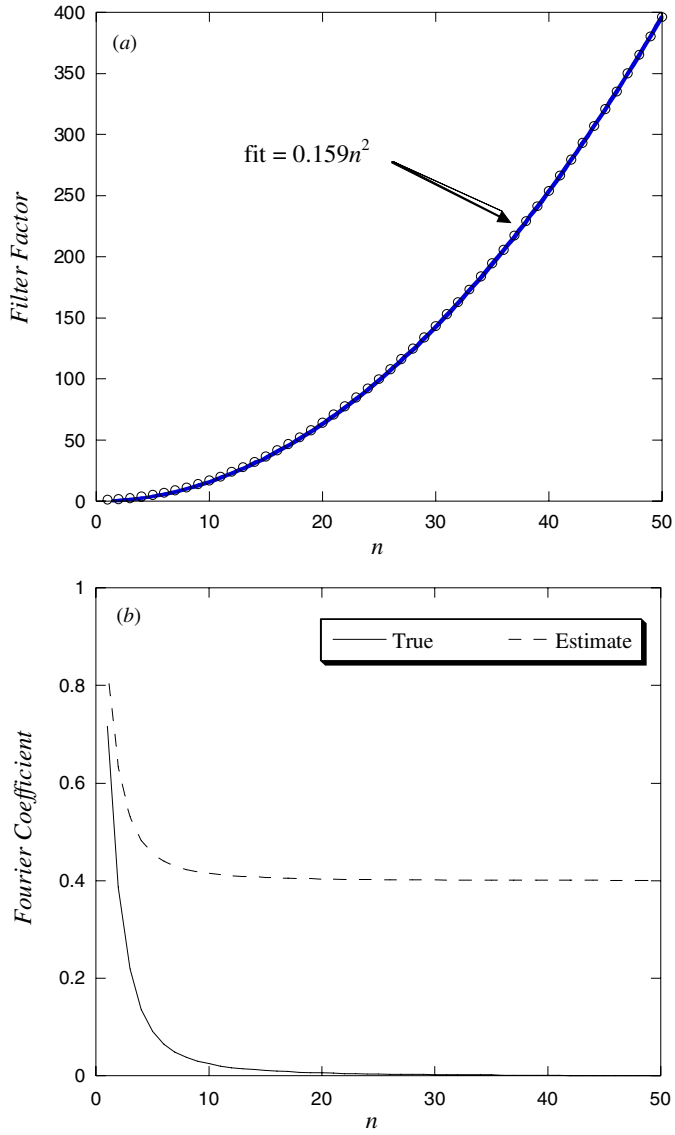

Figure 1. (*a*) Filter factor (right-hand side of equation (A.6)) as a function of harmonic number, n. Circles are data, while the solid line is a quadratic fit to the data. (*b*) Fourier coefficients of the transformed kernels (true kernel is the lower solid curve whereas the estimated kernel is the upper dashed curve). $a = 0.5$, $\eta_0 = 1$ and $\xi = 0.1$.

This linear convolution has a Fourier series expansion valid in the interval $-a \leqslant y < a$. The Fourier coefficients of the convolution are thus

$$\hat{\sigma}_R(n) = \frac{1}{2a}\int_{-a}^{a} \sigma_R(y)\, \mathrm{e}^{-\mathrm{i}\frac{\pi}{a}ny}\, \mathrm{d}y = \frac{1}{2a}\int_{-a}^{a}\int_{-a}^{a} \eta(y-y')R(y')\, \mathrm{e}^{-\mathrm{i}\frac{\pi}{a}ny}\, \mathrm{d}y'\, \mathrm{d}y$$
$$= \frac{1}{2a}\int_{-a}^{a} R(y')\, \mathrm{e}^{-\mathrm{i}\frac{\pi}{a}ny'} \left[\int_{-a-y'}^{a-y'} \eta(s)\, \mathrm{e}^{-\mathrm{i}\frac{\pi}{a}ns}\, \mathrm{d}s\right] \mathrm{d}y'. \tag{B.7}$$

If the true kernel has a valid Fourier transform, then $\eta(s) = \frac{1}{2\pi}\int_{-\infty}^{\infty}\tilde{\eta}(k)\,\mathrm{e}^{iks}\,\mathrm{d}k$, which when substituting into equation (B.7) and performing some manipulations, leads to

$$\hat{\sigma}_R(n) = \frac{1}{2\pi}\int_{-\infty}^{\infty}\tilde{\eta}(k)\left[\frac{1}{2a}\int_{-a}^{a}R(y')\,\mathrm{e}^{-\mathrm{i}\frac{\pi}{a}ny'}\left\{\int_{-a-y'}^{a-y'}\mathrm{e}^{\mathrm{i}(k-\frac{\pi}{a}n)s}\,\mathrm{d}s\right\}\mathrm{d}y'\right]\mathrm{d}k. \tag{B.8}$$

The integral in curly brackets can be evaluated explicitly to give

$$\int_{-a-y'}^{a-y'}\mathrm{e}^{\mathrm{i}(k-\frac{\pi}{a}n)s}\,\mathrm{d}s = \mathrm{e}^{-\mathrm{i}(k-\frac{n\pi}{a})y'}2a\,\mathrm{sinc}((k-n\pi/a)a), \tag{B.9}$$

which, when substituting into equation (B.8) and performing some more algebra, gives

$$\hat{\sigma}_R(n) = \frac{1}{2\pi}\int_{-\infty}^{\infty}\tilde{\eta}(k)\left[\int_{-a}^{a}R(y')\,\mathrm{e}^{-\mathrm{i}ky'}\,\mathrm{d}y'\right]\mathrm{sinc}((k-n\pi/a)a)\,\mathrm{d}k. \tag{B.10}$$

Since the term in the square brackets is just the Fourier transform of the ramp-like input function ($\tilde{R}(k)$) we can express equation (B.10) as

$$\hat{\sigma}_R(n) = \frac{1}{2\pi}\int_{-\infty}^{\infty}\tilde{\eta}(k)\tilde{R}(k)\mathrm{sinc}((k-n\pi/a)a)\,\mathrm{d}k. \tag{B.11}$$

Equation (B.11) gives us the expression for the Fourier coefficients of the linear convolution function $\sigma_R(y)$ defined in equation (B.6). In order to compare this function with the Fourier coefficients of the corresponding circular convolution we first express the circular convolution in terms of the periodic function defined in equation (B.5),

$$\sigma_C(y) = \int_{y-a}^{y+a}\eta_C(y-y')r(y')\,\mathrm{d}y'; \qquad -a \leqslant y < a, \tag{B.12}$$

where now $\eta_C(y)$ is the kernel for the circular convolution and is non-zero only on the interval $-a \leqslant y < a$. This function has a Fourier series expansion valid in $-a \leqslant y < a$ with Fourier coefficients given by

$$\begin{aligned}\hat{\sigma}_C(n) &= \frac{1}{2a}\int_{-a}^{a}\left[\int_{y-a}^{y+a}\eta_C(y-y')r(y')\,\mathrm{d}y'\right]\mathrm{e}^{-\mathrm{i}\frac{n\pi}{a}y}\,\mathrm{d}y \\ &= \int_{-a}^{a}\eta_C(s)\left[\frac{1}{2a}\int_{-a}^{a}r(y-s)\,\mathrm{e}^{-\mathrm{i}\frac{n\pi}{a}(y-s)}\,\mathrm{d}y\right]\mathrm{e}^{-\mathrm{i}\frac{n\pi}{a}s}\,\mathrm{d}s.\end{aligned} \tag{B.13}$$

As the integral in the square brackets is periodic with period $2a$, integrating over any complete period shows that the integral is independent of s and is in fact just the Fourier coefficient of the periodic input ramp-like function, $\hat{r}(n)$. Taking this out of the integral in equation (B.13) shows that the remaining integral is just the Fourier transform of the circular convolution kernel, $\tilde{\eta}_C(k)$, evaluated at harmonics $k = n\frac{\pi}{a}$ of the ramp function. Therefore, equation (B.13) becomes

$$\hat{\sigma}_C(n) = \hat{r}(n)\tilde{\eta}_C(n\pi/a). \tag{B.14}$$

If the true linear and the circular convolutions are equivalent on the interval $-a \leqslant y < a$, then the Fourier coefficients given by equations (B.11) and (B.14) must be equal, in which case

$$\tilde{\eta}_C(n\pi/a) = \frac{1}{2\pi}\int_{-\infty}^{\infty}\tilde{\eta}(k)\frac{\tilde{R}(k)}{\hat{r}(n)}\,\mathrm{sinc}((k-n\pi/a)a)\,\mathrm{d}k. \tag{B.15}$$

This can be expressed in a more useful form by dividing both sides by the sampled values of the Fourier transform of the true kernel and by noting that $\hat{\eta}(n) = \frac{1}{2a}\tilde{\eta}\left(\frac{n\pi}{a}\right)$ on the interval $-a \leqslant y < a$. Similarly, $\hat{r}(n) = \frac{1}{2a}\tilde{R}\left(\frac{n\pi}{a}\right)$ and $\hat{\eta}_C(n) = \frac{1}{2a}\tilde{\eta}_C\left(\frac{n\pi}{a}\right)$, which leads to

$$\frac{\hat{\eta}_C(n)}{\hat{\eta}(n)} = \int_{-\infty}^{\infty}\frac{\tilde{\eta}(k+n\pi/a)}{\tilde{\eta}(n\pi/a)}\frac{\tilde{R}(k+n\pi/a)}{\tilde{R}(n\pi/a)}\frac{a}{\pi}\,\mathrm{sinc}(ka)\,\mathrm{d}k. \tag{B.16}$$

Thus the right-hand side of equation (B.16) essentially gives a filter, which indicates the effect of the processing scheme on the estimated kernel due to the circular convolution inherent in the DFT procedure.

In figure 1(*a*) we plot this filter factor as a function of harmonic number, n, for our test kernel defined in equation (13) with the parameters $a = 0.5$, $\eta_0 = 1$ and $\xi = 0.1$. In figure 1(*b*) we plot the Fourier coefficients for the true and estimated kernels. Of particular interest is that the filter coefficient increases quadratically in n for large n. Bearing in mind that $\tilde{\eta}(k) \sim 1/k^2$ for large k, this implies (from equation (B.16)) that the Fourier coefficients of the circular kernel will asymptote to a finite constant value for large k, rather than to zero as is the case for the true linear kernel. This is seen clearly in figure 1(*b*) in which the Fourier coefficients for the true kernel decay to zero as harmonic number increases, whereas they tend towards a constant non-zero value for the estimated kernel. This is also consistent with the results presented in figure 6. As we have previously observed, this finite value of the k-space kernel leads to a delta-function spike in the estimated real-space kernel at $y = 0$ that in turn distorts the overall shape of the estimated kernel function. Subtraction of the coefficient of the largest harmonic from all other coefficients will result in a real-space kernel that has a similar shape to the true kernel. However, this will give an incorrect value for the integral of the kernel, which is equal to $\tilde{\eta}(k = 0)$. Clearly the subtraction of this large harmonic coefficient should not be performed for all lower harmonic coefficients, but it is not clear at what harmonic numbers this process could be safely applied.

References

[1] Zhang J, Todd B D and P Travis K 2004 *J. Chem. Phys.* **121** 10778
Zhang J, Todd B D and P Travis K 2005 *J. Chem. Phys.* **122** 219901
[2] Travis K P and Gubbins K E 2000 *J. Chem. Phys.* **112** 1984
[3] Evans D J and Morriss G P 1990 *Statistical Mechanics of Nonequilibrium Liquids* (London: Academic)
[4] Travis K P, Todd B D and Evans D J 1997 *Phys. Rev.* E **55** 4288
[5] Todd B D, Evans D J, Travis K P and Daivis P J 1999 *J. Chem. Phys.* **111** 10730
[6] Schiek R and Shaqfeh E S G 1995 *J. Fluid. Mech.* **296** 271
[7] Jurgensen C W and Shaqfeh E S G 1988 *J. Appl. Phys.* **64** 6200
[8] Boon J and Yip S 1980 *Molecular Hydrodynamics* (New York: McGraw-Hill)
[9] Akcasu A Z and Daniels E 1970 *Phys. Rev.* A **2** 962
[10] Ailawadi N K, Rahman A and Zwanzig R 1971 *Phys. Rev.* A **4** 1616
[11] Alley W E and Alder B J 1983 *Phys. Rev.* A **6** 3158
[12] Todd B D, Evans D J and Daivis P J 1995 *Phys. Rev.* E **52** 1627
[13] Travis K P, Searles D J and Evans D J 1999 *Mol. Phys.* **97** 415
[14] Hansen J S, Daivis P J, Travis K P and Todd B D 2007 *Phys. Rev.* E **76** 041121
[15] Weeks J D, Chandler D and Andersen H C 1971 *J. Chem. Phys.* **54** 5237
[16] Zhang J 2005 *PhD Thesis* Swinburne University of Technology (available online at http://www.it.swin.edu.au/centres/cms/)
[17] Gosling E M, McDonald I R and Singer K 1973 *Mol. Phys.* **26** 1475
[18] Baranyai A, Evans D J and Daivis P J 1992 *Phys. Rev.* A **46** 7593
[19] Todd B D, Hansen J S and Daivis P J 2007 in preparation
[20] O'Neil P V 1983 *Advanced Engineering Mathematics* (California: Wadsworth)
[21] For example, see the Mathematica user's guide at: http://documents.wolfram.com/applications/digitalimage/index3.html